



**HAL**  
open science

# Enhancing the Output Voltage of Piezoelectric Nanogenerators Based on ZnO Nanowires Grown by Chemical Bath Deposition Using Compensatory Cu Doping

Manuel Manrique, Vincent Consonni, Sarah Boubenia, Hervé Roussel, Mohammed Zeghouane, Sébastien Labau, Sébastien Cavalaglio, Catherine Pudda, Véronique Jacob, Gwenael Le Rhun, et al.

► **To cite this version:**

Manuel Manrique, Vincent Consonni, Sarah Boubenia, Hervé Roussel, Mohammed Zeghouane, et al.. Enhancing the Output Voltage of Piezoelectric Nanogenerators Based on ZnO Nanowires Grown by Chemical Bath Deposition Using Compensatory Cu Doping. *Energy Technology*, 2024, 12 (5), pp.2301381. 10.1002/ente.202301381 . hal-04509878

**HAL Id: hal-04509878**

<https://hal.univ-grenoble-alpes.fr/hal-04509878v1>

Submitted on 12 Dec 2024

**HAL** is a multi-disciplinary open access archive for the deposit and dissemination of scientific research documents, whether they are published or not. The documents may come from teaching and research institutions in France or abroad, or from public or private research centers.

L'archive ouverte pluridisciplinaire **HAL**, est destinée au dépôt et à la diffusion de documents scientifiques de niveau recherche, publiés ou non, émanant des établissements d'enseignement et de recherche français ou étrangers, des laboratoires publics ou privés.



Distributed under a Creative Commons Attribution 4.0 International License

# Enhancing the Output Voltage of Piezoelectric Nanogenerators Based on ZnO Nanowires Grown by Chemical Bath Deposition Using Compensatory Cu Doping

Manuel Manrique, Vincent Consonni,\* Sarah Boubenia, Hervé Roussel, Mohammed Zeghouane, Sébastien Labau, Sébastien Cavalaglio, Catherine Pudda, Véronique Jacob, Gwenaél Le Rhun, and Bassem Salem\*

The screening effect in ZnO nanowires (NWs) coming from the high density of free electrons has emerged as one of the major issues for their efficient integration into piezoelectric devices. Herein, the compensatory Cu doping of ZnO NWs grown by chemical bath deposition in the high-pH region using  $\text{Cu}(\text{NO}_3)_2$  and ammonia as chemical additives is developed and the effects of a postdeposition thermal annealing under oxygen atmosphere are investigated. It is shown that the Cu dopants are incorporated into ZnO NWs with an atomic [Cu]/[Zn] ratio in the range of 50–65 ppm and undergo a migration process into their bulk after thermal annealing. Importantly, the electrical resistivity of Cu-doped ZnO NWs is found to increase by a factor of 4 compared to unintentionally n-doped ZnO NWs. The increase is even more pronounced after different thermal annealing, reaching a factor exceeding 100, which is explained by the redistribution of hydrogen- and nitrogen-related defects along with the thermal activation of Cu dopants. Additionally, it is revealed that a rigid piezoelectric nanogenerator based on a Cu-doped ZnO NW matrix exhibits the highest output voltage and effective piezoelectric coefficient  $d_{33}^{\text{eff}}$  thanks to the reduction of the screening effect, opening perspectives in the field of piezoelectric devices.

## 1. Introduction


Harvesting energy from nature to develop self-powered nanodevices/nanosystems<sup>[1–6]</sup> has been on the spotlight of the research community over the last years. Unlike renewable energy sources such as light or heat, ubiquitous vibrations from body movement and fluid flow permanently provide mechanical energy whose conversion into electrical energy can be directly achieved by devices based on piezoelectric nanogenerators (PNGs).<sup>[7–9]</sup> Furthermore, the energy conversion efficiency can be enhanced when PNGs are based on an integrated nanowire (NW) matrix.<sup>[10]</sup> Among the different piezoelectric materials, such as GaN,  $\text{BaTiO}_3$ , AlN, or  $\text{Pb}(\text{Zr}_x\text{Ti}_{1-x})\text{O}_3$ , ZnO is a prominent candidate considering its abundancy and biocompatibility for human wearable devices or biomedical diagnostics.<sup>[11–16]</sup> The chemical synthesis of ZnO NWs can be carried out by various

M. Manrique, S. Boubenia, M. Zeghouane, S. Labau, S. Cavalaglio, B. Salem  
Univ. Grenoble Alpes  
CNRS  
CEA/LETI Minatoc  
Grenoble INP  
LTM  
38054 Grenoble, France  
E-mail: bassem.salem@cea.fr

M. Manrique, V. Consonni, H. Roussel  
Univ. Grenoble Alpes  
CNRS  
Grenoble INP  
LMGP  
F-38000 Grenoble, France  
E-mail: vincent.consonni@grenoble-inp.fr

M. Manrique, C. Pudda, G. Le Rhun  
Univ. Grenoble Alpes  
CEA  
LETI  
F-38000 Grenoble, France

V. Jacob  
Univ. Grenoble Alpes  
CNRS  
IRD  
Grenoble INP  
IGE  
F-38000 Grenoble, France

 The ORCID identification number(s) for the author(s) of this article can be found under <https://doi.org/10.1002/ente.202301381>.

© 2024 The Authors. Energy Technology published by Wiley-VCH GmbH. This is an open access article under the terms of the Creative Commons Attribution-NonCommercial License, which permits use, distribution and reproduction in any medium, provided the original work is properly cited and is not used for commercial purposes.

DOI: 10.1002/ente.202301381

techniques,<sup>[17]</sup> the chemical bath deposition (CBD) operating at low temperature (70–90 °C) being one of the most attractive sustainable wet chemical routes.<sup>[18–21]</sup> Nevertheless, the high concentration of intrinsic/extrinsic point defects in ZnO NWs grown by CBD<sup>[22]</sup> severely affects their piezoelectric properties, causing a significant loss of the PNG performances. When a mechanical stress is applied on the top face of ZnO NWs grown along the polar *c*-axis,<sup>[23]</sup> a piezoelectric potential is subsequently generated. At the same time, a migration process of free charge carriers (i.e., free electrons) toward the positive pole of the created electric field takes place, leading to a decrease and/or neutralization of the piezoelectric potential. This phenomenon is known as the screening effect of the piezoelectric potential,<sup>[24–26]</sup> whose magnitude is directly correlated with the density of free charge carriers. In the case of ZnO NWs grown by CBD, for which a high density of free electrons lying in the range of  $5 \times 10^{17}$ – $1.5 \times 10^{19} \text{ cm}^{-3}$  has been measured,<sup>[27–31]</sup> the screening of the piezoelectric potential significantly increases for densities of free electrons exceeding  $10^{18} \text{ cm}^{-3}$ .<sup>[32–34]</sup>

In order to overcome this limitation, many approaches have been carried out including surface O<sub>2</sub> plasma treatment,<sup>[35,36]</sup> p–n junction formation,<sup>[37–39]</sup> thermal treatment,<sup>[40]</sup> and rare-earth element doping.<sup>[41]</sup> Another promising solution relies on the compensatory doping with acceptor atoms, leading to the recombination of electron–hole pairs and then to the reduction of the density of free electrons. Thus, the doping with IA (e.g., Li, Na, K), VA (e.g., N, P, As), and IB (Cu, Ag, Au) group elements has emerged as being a great solution for the integration of ZnO NWs into PNGs.<sup>[42–44]</sup> The acceptors from IA and IB groups substituting for Zn sites present low ionization energies, relative to the valence band maximum, which have been calculated as 90, 170, 320, 200–250, 350, and 450 meV for Li<sub>Zn</sub>, Na<sub>Zn</sub>, K<sub>Zn</sub>, Ag<sub>Zn</sub>, Cu<sub>Zn</sub>, and Au<sub>Zn</sub>, respectively.<sup>[45,46]</sup> In particular, owing to the small ionic radius of IA group elements, they might occupy interstitial sites, requiring a thermal treatment for their activation into substitutional sites.<sup>[47]</sup> Moreover, the doping with VA (e.g., N, P, As) group elements substituting for O sites is expected to be less efficient owing to their higher calculated ionization energies.<sup>[47]</sup> Considering the factors mentioned above, as well as its abundance and cost, Cu has emerged as a great candidate for the compensatory doping of ZnO. A recent work reported that ZnO NWs can be doped by CBD with Cu<sup>[48]</sup> by using copper nitrate as a chemical additive in an aqueous solution containing zinc nitrate and hexamethylenetetramine (HMTA), and by promoting the adsorption and incorporation processes of Cu dopants through the adjustment of the pH of the chemical bath. Moreover, according to *ab initio* calculations, an acceptor energy level in the range of 0.7–1 eV above the valence band maximum of ZnO<sup>[49,50]</sup> is expected for Cu. In the literature, many reports revealed the acceptor behavior of Cu atoms in ZnO nanostructures grown by different methods, but the compensatory Cu doping and its effects on the electrical properties of ZnO NWs grown by CBD and, consequently, on the piezoelectric properties of a PNG based on these nanostructures have not been revealed until now.

In the present work, ZnO NWs are grown by CBD in the high-pH region to evaluate the incorporation process of Cu dopants using Raman spectroscopy, X-ray photoelectron spectroscopy (XPS), and inductively coupled plasma mass spectrometry (ICP-MS) measurements. The effect of the Cu doping and its

thermal activation are assessed through two-point probe electrical resistivity measurements. The influence of the morphology of the vertically integrated ZnO NW matrix grown by CBD and of its Cu doping on the piezoelectric properties of PNGs is eventually decoupled, showing the great promise offered by Cu dopants to drastically enhance the performance of PNGs.

## 2. Results and Discussion

### 2.1. Compensatory Cu Doping and Thermal Annealing Effect on the Physicochemical Properties of ZnO NWs

The doping of ZnO NWs by CBD occurs through the addition of a dedicated chemical precursor containing the dopant (e.g., AlCl<sub>3</sub>,<sup>[51]</sup> Al(NO<sub>3</sub>)<sub>3</sub>,<sup>[52]</sup> Ga(NO<sub>3</sub>)<sub>3</sub>,<sup>[53]</sup> and so on). By carefully adjusting the pH conditions, the adsorption process of dedicated ion complexes on the charged surfaces of ZnO NWs proceeds, resulting in the incorporation process of dopants. When using column-IB dopants like Cu, both electrostatic and chemical forces have been found to play a role to drive the adsorption process in the low- and high-pH regions.<sup>[48]</sup> In the present work, Cu(NO<sub>3</sub>)<sub>2</sub> was used as the chemical additive and the initial pH (pH<sub>0</sub>) of the chemical bath was set to a value of 10.6. In the present high-pH region, Cu(NH<sub>3</sub>)<sub>4</sub><sup>2+</sup> complexes acting as the predominant Cu(II) species are formed and readily adsorbed on the negatively charged top polar *c*-planes of ZnO NWs (pH > 8.7 ± 0.2).<sup>[54]</sup> The incorporation of Cu dopants is thus favorable following the adsorption process of Cu(NH<sub>3</sub>)<sub>4</sub><sup>2+</sup> complexes from electrostatic and chemical forces. Yan et al. further calculated via density functional theory that, under oxygen-rich conditions corresponding to the high-pH region, the Cu dopant can occupy the Zn site as Cu<sub>Zn</sub> acting as an acceptor with a low formation energy.<sup>[49]</sup> Moreover, owing to the expected low supersaturation of Cu(II) species, the precipitation of Cu<sub>2</sub>O and CuO-based residual phases is thermodynamically not favorable.<sup>[48]</sup>

The morphological properties of both unintentionally n- and Cu-doped ZnO NWs grown by CBD with a [Cu(II)]/[Zn(II)]<sub>bath</sub> ratio of 0% and 5%, respectively, are shown in **Figure 1** using field-emission scanning electron microscopy (FESEM) images. An epitaxially vertical growth on the preferentially *c*-axis-oriented polycrystalline ZnO seed layer is observed.<sup>[55]</sup> Concerning their morphological properties, the unintentionally n-doped ZnO NWs have a mean length of 6.7 ± 0.2 μm with tapered shape top faces (Figure 1a,b), while Cu-doped ZnO NWs reach a mean length of 7.3 ± 0.1 μm with flat hexagonal shape top faces (Figure 1c,d). The tapered shape top face results from a high axial growth rate along the polar *c*-axis, which occurs at the expense of the radial growth along the nonpolar *m*-axis.<sup>[48]</sup> On the contrary, the hexagonal flat shape is consecutive to a possible obstruction of the axial growth<sup>[56]</sup> by the adsorption process of Cu(NH<sub>3</sub>)<sub>4</sub><sup>2+</sup> complexes on the polar *c*-plane of ZnO NWs.<sup>[48,54]</sup>

In addition, it is well known that the coexistence of heterogeneous and homogeneous growth processes occurs during the growth of ZnO NWs by CBD (i.e., on the substrate and into the bulk solution, respectively). The dominance of each growth process depends on the solubility of Zn(II) species, which can be modified by the presence of chemical additives. In the present study, as ZnO NWs were grown using a chemical bath with a

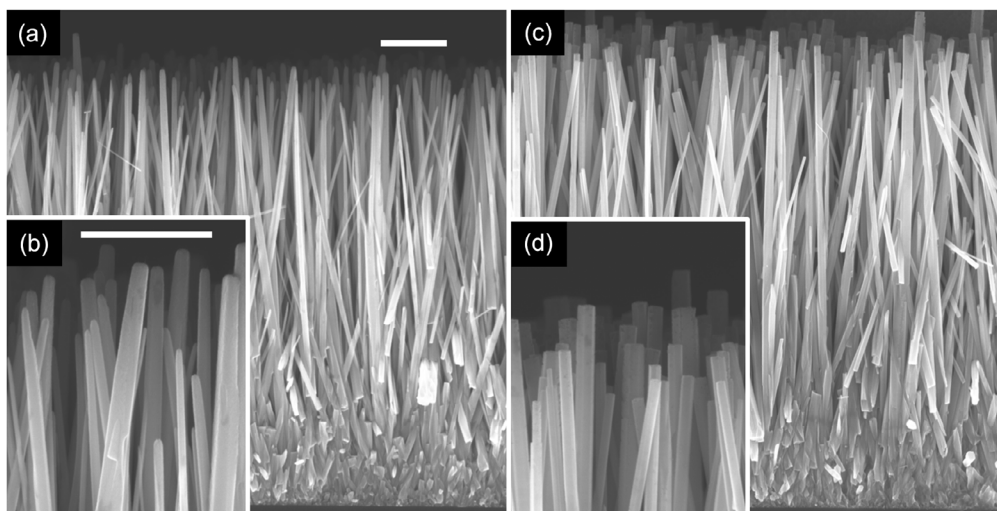


**Figure 1.** Cross-sectional FESEM images of ZnO NWs with a  $[\text{Cu(II)}]/[\text{Zn(II)}]_{\text{bath}}$  ratio of a,b) 0% and c,d) 5%. The scale bar corresponds to 1  $\mu\text{m}$ .

large volume for an extended length of time, the presence of  $\text{NH}_3$  and  $\text{Cu}(\text{NO}_3)_2$  might have a major impact on the depletion of chemical reactants contributing to the heterogeneous growth. Accordingly, the amount of chemical reactants available for the formation of unintentionally n-doped ZnO NWs is expected to be smaller than that of Cu-doped ZnO NWs. This may also account for the different morphologies of n- and Cu-doped ZnO NWs resulting from the different depletion rates of chemical reactants.

Furthermore, neither  $\text{Cu}_2\text{O}$  nor  $\text{CuO}$  nanocrystals are detected when growing Cu-doped ZnO NWs in the present high-pH region.

After different thermal annealing of both unintentionally n- and Cu-doped ZnO NWs, no evolution of their morphological properties occurs. The Raman scattering spectra of as-grown and annealed unintentionally n- and Cu-doped ZnO NWs were recorded in the low wavenumber range from 70 to  $800\text{ cm}^{-1}$  and calibrated from the Si line at  $520.7\text{ cm}^{-1}$ , as shown in **Figure 2a**. The indicative optical phonon modes of the wurtzite structure of ZnO NWs are observed at 99 ( $E_2^{\text{low}}$ ), 380 ( $A_1(\text{TO})$ ),  $\approx 438$  ( $E_2^{\text{high}}$ ), and 574 ( $A_1(\text{LO})$ )  $\text{cm}^{-1}$ .<sup>[57]</sup> The second-order modes are located at 203 ( $2\text{TA}/2 E_2^{\text{low}}$ ), 333 ( $E_2^{\text{high}} - E_2^{\text{low}}$ ), and 483 ( $2\text{LA}$ )  $\text{cm}^{-1}$ . Concerning Cu-doped ZnO NWs, no  $\text{Cu}_2\text{O}$ -,  $\text{CuO}$ -, or  $\text{Cu}(\text{OH})_2$ -related Raman peaks are detected,<sup>[58]</sup> regardless of the thermal annealing used. Furthermore, for both unintentionally n- and Cu-doped ZnO NWs, additional modes (AMs) attributed to dopant-induced defects appear after thermal annealing. They are related to the presence of extrinsic impurities including Al, Ga, N, Sb, and Fe,<sup>[59]</sup> probably coming from the ammonia added in the chemical bath. Villafuerte et al. assigned these AMs to ZnO  $B_1$  silent modes located at 275 ( $B_1^{\text{low}}$ ), 581 ( $B_1^{\text{high}}$ ), and 643 ( $\text{TA} + B_1^{\text{high}}$ )  $\text{cm}^{-1}$ ,<sup>[60]</sup> which become Raman active due to the breakdown of the translational crystal symmetry after thermal annealing.<sup>[61]</sup> Particularly, the increase of the Raman peak around  $580\text{ cm}^{-1}$  for thermal annealing at 300 and  $500^\circ\text{C}$  is the result of the coupling of the two  $B_1^{\text{high}}$  and  $A_1(\text{LO})$  modes owing to their wavenumber proximity. Interestingly, the increase in the intensity of the  $E_2^{\text{high}}$  peak along

with the decrease of its full width half maximum, as the annealing temperature is increased, reveals an improvement of the crystallinity of unintentionally n- and Cu-doped ZnO NWs after thermal annealing, as depicted in **Figure 2b**. Additionally, the position of the  $E_2^{\text{high}}$  peak shifts to lower wavenumber as the annealing temperature is increased, indicating a possible relaxation of the residual stress along the  $c$ -axis of the wurtzite structure of ZnO NWs.<sup>[62,63]</sup> For unintentionally n-doped ZnO NWs, the  $E_2^{\text{high}}$  peak significantly shifts from  $437.7\text{ cm}^{-1}$  (as-grown) to  $436.8\text{ cm}^{-1}$  ( $800^\circ\text{C}$ ), which probably originates from the redistribution of hydrogen- and nitrogen-related defects through the thermal annealing.<sup>[60]</sup> For Cu-doped ZnO NWs, the  $E_2^{\text{high}}$  peak slightly shifts from  $437.8\text{ cm}^{-1}$  (as-grown) to  $437.3\text{ cm}^{-1}$  ( $300^\circ\text{C}$ ), from which a plateau is reached. Interestingly, Cu is expected to preferentially occupy Zn sites to form  $\text{Cu}_{\text{Zn}}$  owing to its similar ionic radius of 74 pm ( $\text{Zn}^{2+}$ ), 77 pm ( $\text{Cu}^{1+}$ ), and 73 pm ( $\text{Cu}^{2+}$ ).<sup>[56,64]</sup> This leads to a distortion of the lattice of ZnO NWs,<sup>[62]</sup> and consequently a possible modification of the Raman line shape induced by a change of phonon contribution, as explained by Samanta et al. through the alloy potential fluctuation within a phonon confinement model.<sup>[65]</sup>

XPS spectra centered on the Cu  $2p$  core level, as presented in **Figure 2c**, reveal the Cu  $2p_{1/2}$  and Cu  $2p_{3/2}$  peaks pointed at 952.5 and 932.7 eV, respectively, of Cu-doped ZnO NWs after thermal annealing. The XPS spectra confirm that neither  $\text{Cu}_2\text{O}$  nor  $\text{CuO}$  residual phases are formed because no prominent satellite peaks in the range of 940–944 eV are detected,<sup>[66]</sup> which is in agreement with Lausecker et al.<sup>[48]</sup> Concerning the Cu  $2p_{3/2}$  peak, owing to its weak intensity, it is difficult to accurately evaluate the Cu oxidation state. Indeed, the Cu  $2p_{3/2}$  peak could be the contribution of Cu(0), Cu(I), or Cu(II) centered at 932.63, 932.18, and 933.11, respectively.<sup>[66]</sup> Moreover, the contribution of each Cu oxidation state can depend on the thermal annealing. For instance, Sultana et al. studied the structural properties of  $\text{CuO}$  thin films after different annealing at 250, 550, and  $850^\circ\text{C}$  for 10 min under Ar atmosphere, and showed that the Cu  $2p_{3/2}$  peak intensity is mainly related to an evolution of the Cu(II) contribution.<sup>[67]</sup> The latter is high for as-deposited films, then severely decreases



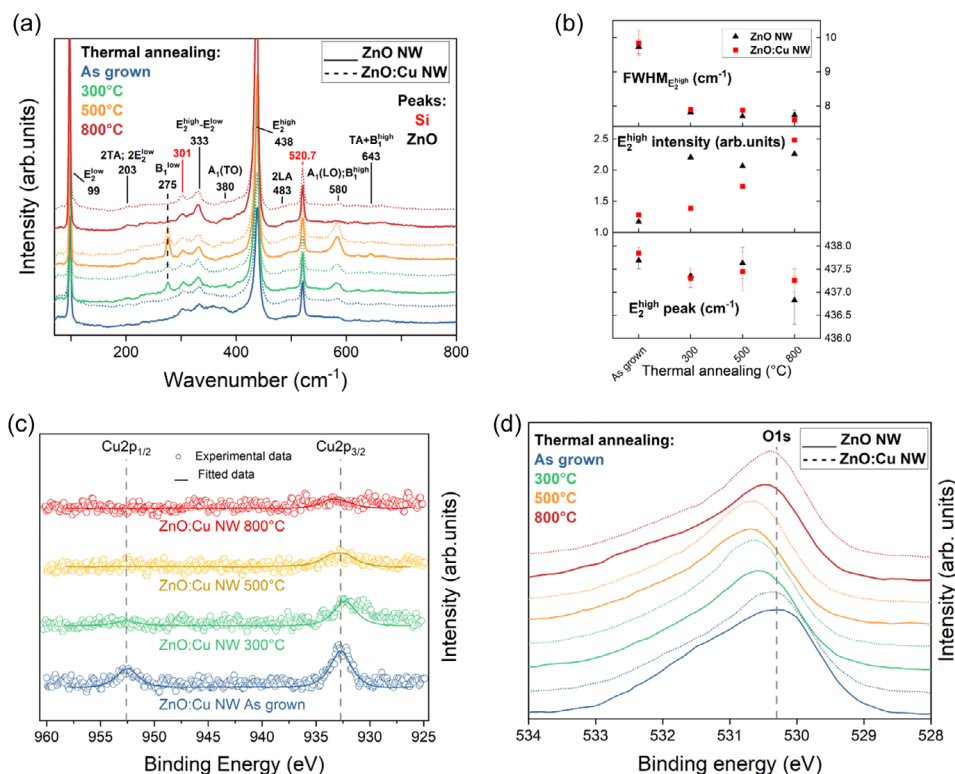


**Figure 2.** a) Raman spectra, b)  $E_2^{\text{high}}$  Raman peak evolution, c) XPS spectra centered on the Cu 2p, and d) O 1s core levels of unintentionally n- and Cu-doped ZnO NWs after thermal annealing at different temperatures under  $O_2$  atmosphere.

until 550 °C, and finally increases at 880 °C, while the Cu(0)/Cu(I) contribution remains almost constant regardless the thermal annealing. Another work conducted by Garces et al. confirmed a change of the oxidation state from Cu(I) to Cu(II) after a thermal annealing for 1 h at 900 °C in ZnO crystal with trace of Cu.<sup>[68]</sup> From these studies, in order to evaluate the possibility of a modification of the oxidation state of Cu, the O 1s and Zn  $2p_{3/2}$  core levels were fitted for both unintentionally n- and Cu-doped ZnO NWs after thermal annealing, as shown in Figure 2 and S1, Supporting Information, respectively. A clear shift of the O 1s (530.3 eV) as well as the Zn  $2p_{3/2}$  (1021.6 eV) peaks toward higher energies is observed as a function of the thermal annealing. This could be the result of an enrichment of hydroxyl groups in surface of ZnO NWs, resulting from an exodiffusion process of hydrogen,<sup>[40]</sup> as explained by Gaffuri et al.<sup>[69]</sup> In this context, a bonding in the form of Cu(OH)<sub>2</sub> (Cu(II)) with two peaks at 933.1 and 934.5 eV in the Cu  $2p_{3/2}$  range could be expected in our samples.<sup>[66]</sup> Then, given the fact that the present XPS measurements are recorded from data provided up to about 5 nm below the surface of Cu-doped ZnO NWs, the decrease in the intensity of the Cu  $2p_{3/2}$  peak highlights a reduction of the amount of Cu at their surfaces after thermal annealing. Furthermore, an ICP-MS analysis quantifying the amount of Cu in the bulk of ZnO NWs reveals that the atomic [Cu]/[Zn] ratio lies in the range of 50–65 ppm and hence remains stable before and after annealing. By considering six atoms of Zn in one hexagonal crystallographic cell, i.e.,  $4.2 \times 10^{22}$  at  $\text{cm}^{-3}$  of Zn, we could expect  $2.1\text{--}2.7 \times 10^{18}$  at  $\text{cm}^{-3}$  of Cu, regardless

the thermal annealing used (Figure S2, Supporting Information). The combination of FESEM, Raman scattering, XPS, and ICP-MS studies shows the successful incorporation of Cu dopants into ZnO NWs, following the approach developed by Lausecker et al.<sup>[48]</sup> and suggests that Cu dopants may exhibit different oxidation states in the ZnO NWs after thermal annealing.

## 2.2. Compensatory Cu Doping and Thermal Annealing Effect on Electrical Properties of ZnO NWs

The electrical properties of unintentionally n- and Cu-doped ZnO NWs were assessed using a two-point probe electrical resistivity measurement through the bottom transistor devices, whose architecture and realization are shown in Figure 3a,b, respectively. The ZnO NWs were first sonicated in isopropyl alcohol and then dispersed onto a  $p^{++}$  Si(100) wafer covered with a  $\text{Si}_3\text{N}_4$  insulating layer. Then, the optical lithography process was used to define the electrode contacts. After development of the photoresist, the contacts were obtained by the deposition of a metallic stack of 100 nm thick Ti layer and 300 nm thick Au layer using an e-beam evaporator, followed by a lift-off process. The current  $I$  at room temperature and under ambient atmosphere was measured by applying a voltage  $V$  sweeping from  $-1$  to  $+1$  V between the two metallic contacts, resulting in the typical  $I$ - $V$  curve shown in Figure 3c. Eventually, the resistance  $R$  of each ZnO NW was obtained from the slope of the linear  $I$ - $V$  curves.

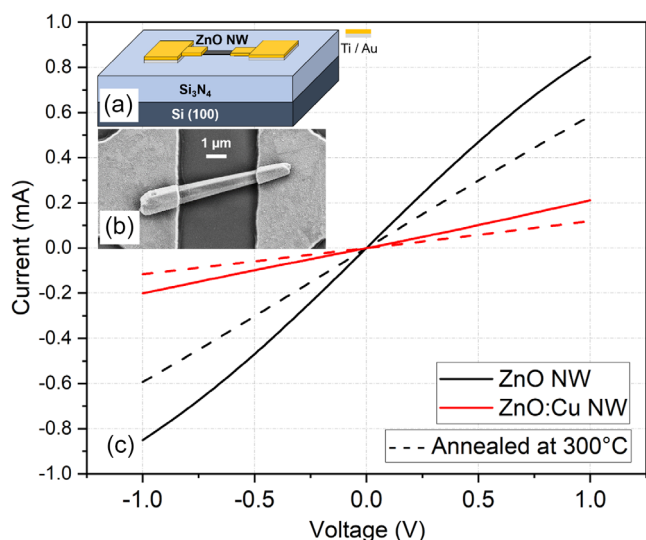


**Figure 3.** a) Schematic of a single ZnO NW contacted bottom transistor. b) Top-view FESEM image of a contacted ZnO NW. c) Typical  $I$ - $V$  curves for an as-grown and annealed unintentionally n-doped ZnO NW and for an as-grown and annealed Cu-doped ZnO NW.

The statistical analysis of the resistance  $R$  over the segment  $l$  (referring to the length between the two metallic contacts of  $\approx 4 \mu\text{m}$ ) of the contacted ZnO NW was performed as a function of its radius  $r$ . The deduced  $R/l$  values were compared with experimental data recorded using a four-point probe resistivity measurement on ZnO NWs grown by metal-organic chemical vapor deposition (MOCVD), carbothermal reduction, hydrothermal process, and CBD in the low-pH region, as shown in **Figure 4a**. There exists a dependence of  $R/l$  values as on  $r$ , regardless of the chemical synthesis. The electrical conduction can be driven by two different mechanisms in the ZnO NWs: when  $r$  is smaller than  $25 \text{ nm}$ ,<sup>[31,70]</sup> a surface electron depletion region resulting from chemisorption processes of  $\text{O}_2^-$  and  $\text{OH}^-$  ions<sup>[70–73]</sup> occurs and leads to higher  $R/l$  values; in contrast, when  $r$  is above  $25 \text{ nm}$ , a bulk-like electrical conduction in a flat-band

regime dominates, where electrons flow through the core of the ZnO NW.

Following this claim, Villafuerte et al.<sup>[22]</sup> delimited the bulk-like electrical conduction region for ZnO NWs grown by CBD, where the  $R/l$  values are proportional to  $1/r^2$ , as shown by the dashed lines in Figure 4a. For the present work, the as-grown unintentionally n- and Cu-doped ZnO NWs exhibit  $R/l$  values inside this region. Then, a clear variation of  $R/l$  values is observed as a function of the annealing temperature. For unintentionally n-doped ZnO NWs, the  $R/l$  values progressively increase from  $2.0 \times 10^2$  to  $1.3 \times 10^6 \Omega \mu\text{m}^{-1}$  as the annealing temperature reaches  $800^\circ\text{C}$ . The same trend is noticed for Cu-doped ZnO NWs, but the  $R/l$  values ranging from  $1.2 \times 10^3$  to  $8.9 \times 10^8 \Omega \mu\text{m}^{-1}$  are systematically higher for each annealing temperature.

The electrical resistivity  $\rho$  was estimated through the equation  $\rho \cong R \frac{S}{l}$ , where  $S$  is the effective electrical conduction section of the NW. The last parameter can be written as  $S = \pi r^2$ , for which a bulk-like electrical conduction is considered.<sup>[71]</sup> As expected from the plot of  $R/l$  values as a function of  $r$ , the electrical resistivity of ZnO NWs increases with the thermal annealing, as presented in Figure 4b. The  $\rho$  mean value for unintentionally n-doped ZnO NWs is of  $4.8 \text{ m}\Omega \text{ cm}$ , and continuously increases from  $1.7 \times 10^1 \text{ m}\Omega \text{ cm}$  through  $1.8 \times 10^3$  to  $1.6 \times 10^4 \text{ m}\Omega \text{ cm}$  for annealing temperatures of  $300$ ,  $500$ , and  $800^\circ\text{C}$ , respectively. As for Cu-doped ZnO NWs, the  $\rho$  mean value is higher and of  $20.2 \text{ m}\Omega \text{ cm}$ , and continuously increases from  $3.1 \times 10^2 \text{ m}\Omega \text{ cm}$  through  $1.4 \times 10^5$  to  $1.7 \times 10^7 \text{ m}\Omega \text{ cm}$  for annealing temperature of  $300$ ,  $500$ , and  $800^\circ\text{C}$ , respectively. The parameters needed for calculating the  $\rho$  value are shown in detail in Figure S3, Supporting Information.

It is well known that the two-point probe method could induce an apparent higher electrical resistivity as result of the occurrence of a significant contact resistance. In the present work, we assume a lower contact resistance for as-grown ZnO NWs because their obtained  $R/l$  values lie in the same region as those reported using the four-point probe method on ZnO NWs grown by CBD in ref. [31]. Then, a progressive increase in the contact resistance following the thermal annealing is expected, reaching its largest influence on the electrical characterizations of

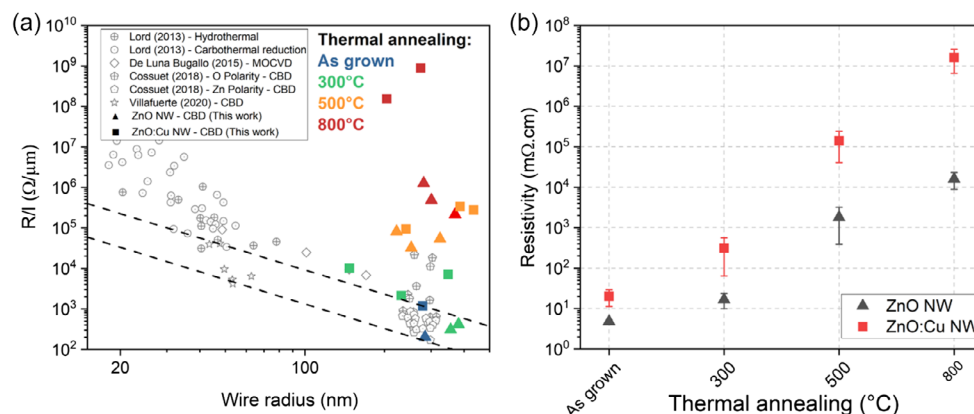


**Figure 4.** a)  $R/l$  values versus  $r$  for the present work and as compared to experimental data reported on ZnO NWs grown by chemical synthesis: hydrothermal process,<sup>[28]</sup> carbothermal reduction,<sup>[28]</sup> MOCVD,<sup>[71]</sup> and CBD<sup>[22,31]</sup> in the low-pH region (image inspired from ref. [22]). b) Electrical resistivity of unintentionally n- and Cu-doped ZnO NWs for different thermal annealing under  $\text{O}_2$  atmosphere during 1 h.

Cu-doped ZnO NWs annealed at 800 °C, which present the highest  $\rho$  values. Following this hypothesis, only these NWs were measured using a four-point probe method, as shown in Figure S4, Supporting Information, revealing a decrease in the  $\rho$  value by a factor of 100. It is worth noticing that, after the thermal annealing at 800 °C, the four-point probe measured electrical resistivity of Cu-doped ZnO NWs is still higher than the initially overestimated electrical resistivity of unintentionally n-doped ZnO NWs assessed by the two-point probe method. The present observation implies that the evolution of electrical resistivity involves an additional factor beyond the influence of the contact resistance.

Given that the morphological properties are not affected by the different thermal annealing (see Figure S5, Supporting Information), the continuous increase in the electrical resistivity for both unintentionally n- and Cu-doped ZnO NWs with the annealing temperature is associated with a redistribution of hydrogen-related defects and Cu dopants in their bulk. Villafuerte et al. showed that the interstitial hydrogen in bond-centered site ( $H_{BC}$ ) and zinc vacancy–hydrogen ( $V_{Zn}-3H$ ) defect complex, both of them with a low formation energy, act as the dominant shallow donors in ZnO NWs grown by CBD.<sup>[22]</sup> In contrast, the  $V_{Zn}-N_O-H$  defect complex with a moderate formation energy behaves as a deep acceptor.<sup>[40]</sup> These hydrogen-related defects mainly modulate the optical and electrical properties of ZnO NWs, and their nature and concentration further depend on the thermal annealing<sup>[40]</sup> and pH<sup>[55]</sup> conditions. For both unintentionally n- and Cu-doped ZnO NWs grown by CBD in the high-pH region and thus under oxygen-rich conditions, the high concentrations of  $H_{BC}$ ,  $V_{Zn}-3H$  and  $V_{Zn}-N_O-H$  defects are expected.<sup>[55]</sup> This leads to the high values for the free charge carrier density and consequently to the low values for the electrical resistivity presented in Figure 4b. Then, by increasing the annealing temperature under  $O_2$  atmosphere, the  $V_{Zn}-3H$  defect complexes dissociate and the  $H_{BC}$  defects undergo an ex-diffusion process, while the  $N_O-H$  and  $V_{Zn}-N_O-H$  defect complexes are progressively formed and activated.<sup>[40]</sup> This leads to a decrease in the free charge carrier density and hence to a continuous increase in the electrical resistivity as presented in Figure 4b. However, the Cu-doped ZnO NWs systematically exhibit higher  $\rho$  mean values regardless of the annealing temperature, indicating the occurrence of additional physical phenomena. This could be explained by the combination of 1) an effective incorporation and migration process of Cu dopants into the bulk of ZnO NWs as revealed by Raman spectroscopy, XPS, and ICP-MS; 2) a change of the oxidation state of the Cu dopants; and 3) a possible thermal activation of the Cu dopants. West et al. demonstrated the formation of deep  $\{Cu_{Zn}^+(3d^{10})-Zn_i^+(4s^1)\}^0$  defect complexes through the association of  $[Cu_{Zn}^+(3d^{10})]^-$  acceptor defects with intrinsic  $Zn_i^+(4s^1)$  donor defects using magneto-optical photoluminescence studies.<sup>[74]</sup> The formation of these defect complexes, coupled to a migration process activated by thermal annealing, could lead to an increase in the electrical resistivity of ZnO NWs.<sup>[75,76]</sup> For instance, Hsu et al. reported that a Cu doping process can introduce a low density of free holes in ZnO NWs when grown by vapor phase transport, resulting in a decrease of the density of free electrons and consequently in an increase of the electrical resistivity.<sup>[64]</sup> For the present work, a similar behavior is expected for as-grown

Cu-doped ZnO NWs, which could explain the higher electrical resistivity measured as compared to unintentionally n-doped ZnO NWs. Second, the thermal energy ( $\approx k_B T - k_B$ : Boltzmann's constant) transferred to the Cu-doped ZnO NWs during the thermal annealing is of 49.3, 66.5, and 92.3 meV as the annealing temperature is set to 300, 500, and 800 °C, respectively. A previous work from Pan et al. showed that the Cu acceptor has an ionization energy of 53 meV, which is reached by an increase of the valence band maximum level of ZnO by sulfur (S) alloying, resulting in a decrease of the bandgap energy ( $\approx 3.2$  eV) as well as the acceptor Cu level.<sup>[77]</sup> Then, given the fact that ZnO NWs grown at  $pH_0 \approx 10.6$  present a bandgap energy around 3.24 eV,<sup>[53]</sup> a thermal activation of Cu dopants inside the Cu-doped ZnO NWs may proceed, leading to the higher values for the electrical resistivity. Finally, the electrical resistivity gap between unintentionally n- and Cu-doped ZnO NWs progressively increases with the temperature annealing, suggesting more efficient electron–hole pair recombination induced by Cu dopants and thus a reduction of the density of free charge carriers. Following this idea, the mean charge carrier density  $n$  was estimated from the  $\rho$  mean values through the equation  $n = \frac{1}{q\mu_{NW}\rho}$ , where  $q$  is the absolute value of the electron charge ( $1.6 \times 10^{-19}$  C) and  $\mu_{NW}$  refers to the electron mobility. For as-grown unintentionally n-doped ZnO NWs, the  $\mu_{NW}$  value reported from longitudinal optical phonon–plasmon coupled modes using Raman spectroscopy was found to lie in the range of  $30\text{--}60$  cm<sup>2</sup> V<sup>-1</sup> s<sup>-1</sup>.<sup>[40]</sup> Consequently, the  $n$  value is found to be around  $3 \times 10^{19}$  cm<sup>-3</sup>. For as-grown Cu-doped ZnO NWs, the  $n$  value could be around  $1.5 \times 10^{19}$  cm<sup>-3</sup> by considering the  $\mu_{NW}$  value as lying in the range of  $15\text{--}30$  cm<sup>2</sup> V<sup>-1</sup> s<sup>-1</sup>.<sup>[64,78–81]</sup> By assuming that the critical concentration  $n_c$  for the Mott transition separating the nonmetal/insulator versus metal electrical conduction regimes is  $4.2 \times 10^{18}$  cm<sup>-3</sup>,<sup>[82]</sup> both the considered unintentionally n- and Cu-doped ZnO NWs exhibit a metallic electrical conduction before thermal annealing, for which the mean charge carrier density exceeds  $10^{19}$  cm<sup>-3</sup>.

### 2.3. Cu Doping Effect on Performances of a ZnO NW-Based PNG

The PNG fabrication process is described in Figure 5a. ZnO NWs were grown by CBD on  $2.5 \times 2$  cm<sup>2</sup> Si substrate covered by a stack of a ZnO seed layer and a bottom electrode (50 nm thick Au layer over 10 nm thick Ti layer) deposited by dip-coating and e-beam evaporation, respectively (1). Then, the ZnO NW matrix was encapsulated by a parylene-C layer, which was deposited by vacuum deposition and polymerization process according to the Gorham method (2).<sup>[83]</sup> The  $1 \times 1$  cm<sup>2</sup> top electrode assisted by a mask was obtained by the stack of three metallic layers: 20 nm thick of Ti layer, 250 nm thick of Al layer, and 100 nm thick of Au layer using e-beam evaporator (3). Finally, both the bottom and top electrodes were contacted by two Cu wires using a conductive resin (4). As a comparison, some PNGs were encapsulated with PDMS to protect them from external natural factors.

Two different PNGs were fabricated according to the  $[Cu(II)]/[Zn(II)]_{bath}$  ratio of 0% and 5% in the chemical bath for the CBD of unintentionally n- and Cu-doped ZnO NW matrix (PNG-A and

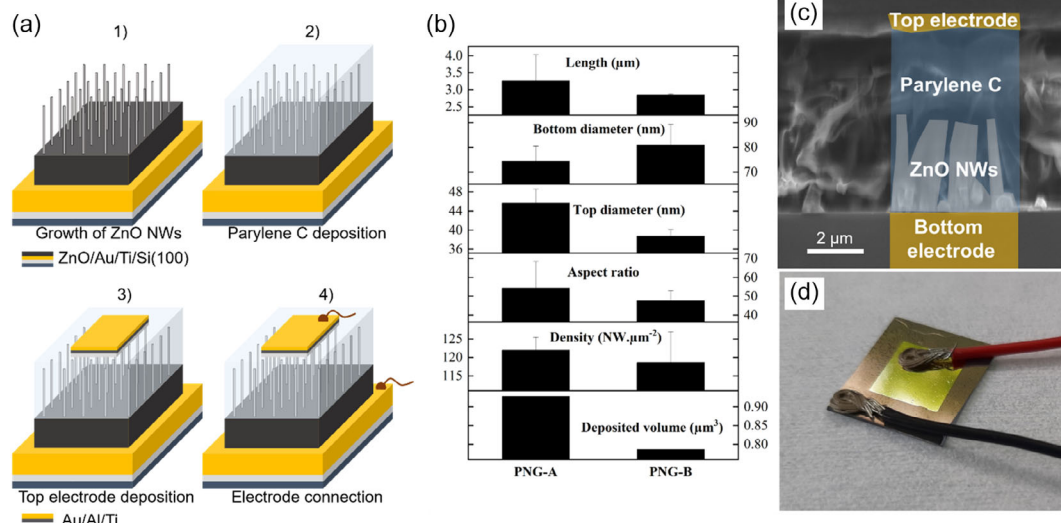


**Figure 5.** a) Fabrication steps of a PNG, b) morphological properties of the integrated ZnO NW matrix with  $[\text{Cu}(\text{II})]/[\text{Zn}(\text{II})]_{\text{bath}}$  ratio of 0% (PNG-A) and 5% (PNG-B), c) cross-sectional FESEM image, and d) picture of a final ZnO NW-based PNG device.

PNG-B, respectively). The CBD was performed in the high-pH region with a  $\text{pH}_0$  value of 10.6 for 3 h at 85 °C. Furthermore, it is worth mentioning that a reference-PNG (without ZnO NW) was also manufactured in order to reveal a possible piezoelectric contribution from the parylene-C layer.

The morphological properties of the vertically integrated ZnO NW matrix are shown and summarized in Figure 5b. The PNG-A has an integrated unintentionally n-doped ZnO NW matrix with the higher mean density ( $122\text{--NW}\cdot\mu\text{m}^{-2}$ ), larger aspect ratio (defined as the ratio between the length divided by the diameter; in this case 54), and higher deposited volume ( $0.9\mu\text{m}^3$ ). The PNG-B has an integrated Cu-doped ZnO NW matrix, for which the mean density, aspect ratio, and deposited volume are of  $118\text{ NW}\cdot\mu\text{m}^{-2}$ , 47, and  $0.78\mu\text{m}^3$ , respectively. In addition, the conformity of the parylene-C layer deposited on these devices, i.e., a good isolation of the NW matrix along with a top dielectric layer allowing a capacitive contact between the top of the NW and the top electrode, was verified as shown in Figure 5c. Furthermore, no short-circuit was detected on any final device (Figure 5d) by measuring an internal impedance value higher than  $10\text{ M}\Omega$  for both PNG-A and PNG-B.

In order to characterize the piezoelectric properties, a vertical force was applied over an area of around  $0.2\text{ cm}^2$  on the top electrode of the PNG through a mechanical shaker. The latter was connected to a force conditioner device that provides an electrical signal (force sensor) as a function of the applied force and time. This electrical signal and the generated piezoelectric signal (piezosignal) by the PNG were simultaneously measured with an oscilloscope, as shown in Figure 6a. Moreover, by keeping constant the distance between the PNG and the shaker for all the piezoelectric characterizations, the mechanical compression cycle was controlled by the frequency and magnitude of a sinus-mode power supplier of the mechanical shaker. Concerning the piezoelectric signal, three different regimes are observed.<sup>[84]</sup> Initially, the beginning of the mechanical compression leads to a fast polarization of the ZnO NW matrix of the PNG

(i.e. the creation of an electric dipole inside a bent NW), resulting in an appearance of external charges in the electrodes and thus a positive voltage peak is achieved. Subsequently, an electrostatic interaction between the positive pole of the created polarization and the free charge carriers inside the ZnO NWs occurs (i.e. the screening effect), reducing the polarization as long as the mechanical deformation time decreases (in other words when the mechanical compression reaches its highest magnitude), and hence reducing in this way the external charges in the electrodes until the total neutralization of the piezoelectric polarization, for which no charges are generated and the voltage plummet as consequence. Eventually, at the end of the compression cycle (release), the same charge creation and transfer occurs in the other way, inducing a symmetrical opposite voltage.

The applied vertical force over the PNG was determined from the force sensor signal by calculating the compression cycle momentum (integration of the force sensor signal) divided by the compression cycle duration. In addition, the PNGs were tested in both forward and reverse connection to confirm a real piezoelectric signal from the signal inversion achieved by reversing the connection polarity. Ideally, the piezoelectric signal must be symmetric when changing the polarity connection of the PNGs; however, the test bench used was not equipped to characterize PNGs in open-circuit conditions, leading to lower piezoelectric signals in reverse connection, as shown in Figure S6, Supporting Information. As a result, only the forward-connection data are shown in the present work. From reference-PNG characterizations, we confirm that the obtained output voltage is due to the piezoelectric phenomenon from ZnO NWs. Thus, PNG-A and PNG-B were characterized under low forces ( $0.5\text{--}5\text{ N}$ ) and low frequency ( $0.5\text{--}5\text{ Hz}$ ) as they are the typical mechanical and frequency ranges present in daily life (people walking,<sup>[85]</sup> human breathing and heart beating,<sup>[86]</sup> soft finger tapping,<sup>[87]</sup> etc.), i.e., lower mechanical stress and frequencies. As expected, according to the mathematical description of the piezoelectric effect (coupling between Hooke and electric



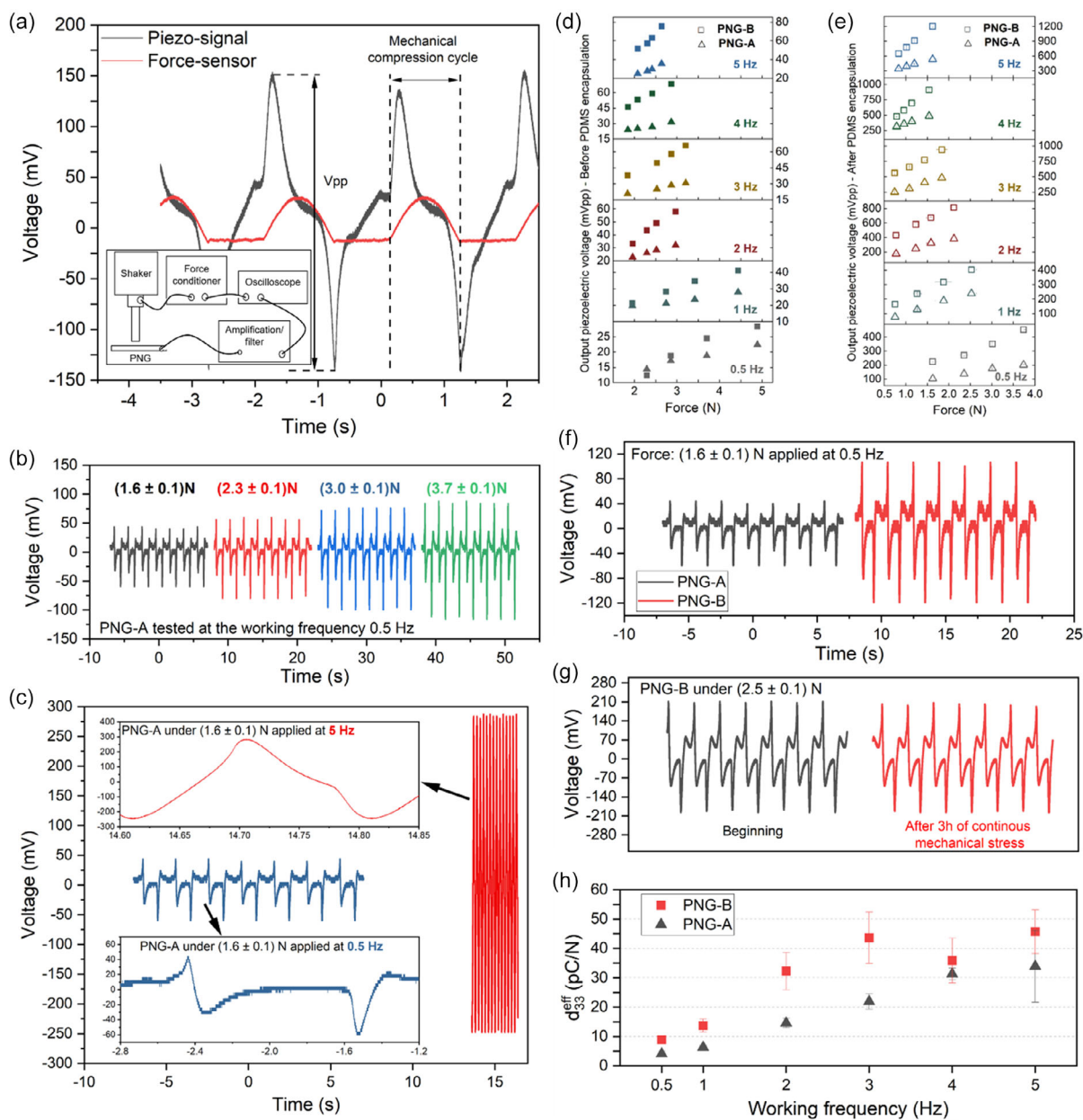


**Figure 6.** a) Piezoelectric characterization of a PNG along with the test bench schematic (inset). b) Output voltage of PNG-A as a function of applied force at 0.5 Hz, and c) as a function of working frequency at constant applied force of 1.6 N. Summary of output voltages of PNG-A and PNG-B d) before and e) after PDMS encapsulation, under different applied forces and working frequencies. f) Output voltage comparison between both PNGs under the same applied force condition. g) Durability of the PNG-B under 2.5 N applied at 1 Hz for 180 min. h) Effective piezoelectric coefficient  $d_{33}^{\text{eff}}$  calculated from piezoelectric signal of PNG-A and PNG-B as a function of working frequency.

displacement field equations), a progressive increment of the piezoelectric signal is obtained as long as the mechanical stress increases (i.e., the compressing force), as shown in Figure 6b and S7, Supporting Information for PNG-A and PNG-B, respectively. Furthermore, the piezoelectric signal exhibits a direct correlation with the working frequency, as revealed in Figure 6c. Indeed, a current ( $I$ ) will be generated according to the equation:  $I = \frac{\Delta Q}{\Delta t} = d_{33} \times A \times \frac{\Delta \sigma}{\Delta t}$ , where  $\Delta Q$  is the charge generated under a mechanical stress ( $\Delta \sigma$ ) applied over an

area ( $A$ ) of a material with a piezoelectric coefficient ( $d_{33}$ ).<sup>[88]</sup> It is worth noticing here that  $Q$  only varies with  $\sigma$ . By increasing the working frequency (i.e., by decreasing  $\Delta t$ ), the strain rate ( $\frac{\Delta \sigma}{\Delta t}$ ) of the ZnO NW matrix increases along with the generated current  $I$  flowing in the external load ( $R_{\text{load}}$ ), i.e., in the amplifier/filter system of the test bench shown in Figure 6a (inset). Subsequently, according to the Ohmic law  $I = R_{\text{load}} V$ , an increase in the piezoelectric voltage ( $V$ ) occurs, as reported in refs. [89,90]. The output voltage obtained for different applied forces at

different working frequencies of the PNG-A and PNG-B, before and after encapsulation with PDMS, are summarized in Figure 6d,e, respectively. Interestingly, the PNGs exhibit higher piezoelectric signals after a PDMS encapsulation, displaying minimum values of about 100 mVpp and maximum values of more than 1 Vpp, regarding the highest signal of about 80 mVpp without encapsulation. The improvement of the output voltage could be attributed to a coupling between piezoelectric and triboelectric effects, the latter induced by the friction between the PDMS layer and metallic top electrode of the PNG. However, it is worth mentioning that the mechanical shaker arm was carefully isolated with a 5 mm thick cardboard piece to minimize a possible triboelectric effect when applying the mechanical stress. A reference-PNG (i.e., without any ZnO NWs but only parylene-C between the two electrodes) with PDMS encapsulation was characterized as well, giving a maximum electrical signal of  $\approx 20$  mVpp, response that was not observed before encapsulation, whose value, however, remains lower than the piezoelectric signal values of PNG-A and PNG-B. Furthermore, regardless of the test condition and PDMS encapsulation, despite PNG-A presents a better ZnO NW matrix morphology for piezoelectric effect (i.e., slightly higher aspect ratio and density), PNG-B provides higher piezoelectric signals that are stable over time, as shown in Figure 6f,g, respectively, and the gap becomes greater as a function of working frequency. These findings thus indicate an additional beneficial effect involving the Cu doping. In order to elucidate this effect, the effective piezoelectric coefficient  $d_{33}^{\text{eff}}$  of the device was calculated by using the approach developed by Lopez Garcia et al. This considers the PNG as a capacitor ( $C_0$ ) discharging over a resistive external load  $R_{\text{load}}$  (corresponding

to the input impedance of the amplifier/filter equipment connected to the PNG—100 M $\Omega$ ), allowing us to write  $d_{33}^{\text{eff}}$  as  $C_0 \times V/F_{\text{applied}}$ , where  $V$  and  $F_{\text{applied}}$  are the generated voltage and applied force, respectively.<sup>[91]</sup> In the present work,  $C_0$  was calculated from the time constant  $\tau$  ( $\tau = C_0 \times R_{\text{load}}$ ) determined by fitting the exponential decay piezoelectric voltage, as shown in Figure S8, Supporting Information. Therefore, the  $d_{33}^{\text{eff}}$  coefficients of PNG-A and PNG-B are shown in Figure 6h as a function of working frequency, whose values at 0.5 and 1 Hz are in the same range with values reported in the literature.<sup>[92,93]</sup> Given the fact that  $d_{33}^{\text{eff}}$  does not depend on the applied force and on the output voltage,<sup>[91]</sup> the observed increase of these values with the working frequency could be the result of a progressive rise of generated current during the mechanical compression cycle, leading to higher output voltages.<sup>[89,90]</sup> Interestingly, PNG-B exhibits higher  $d_{33}^{\text{eff}}$  values than PNG-A, regardless of the working frequency.

The reported piezoelectric coefficient improvement is in agreement with Raman spectroscopy, XPS, ICP-MS, and resistivity measurements: Cu dopants are incorporated into ZnO NWs and decrease their density of free electrons by hole–electron pair recombination,<sup>[48,64]</sup> resulting in an increase of the electrical resistivity and thus a strong reduction of the screening effect,<sup>[24,32,34]</sup> as shown in Figure 7. Then, more external charges are generated during the mechanical stress cycle, leading to an improvement of the  $d_{33}^{\text{eff}}$  coefficient as well as the output voltage. Thus, the ecofriendly low-temperature CBD method, which successfully forms ZnO NWs doped with Cu, opens up: 1) new pathways for enhanced flexible/rigid PNG fabrication, and 2) interests on the morphological, optical, and electrical properties of ZnO NWs with a different range of Cu doping.

(a)  $n_e^{\text{ZnO NWs}} = 3 \times 10^{19} \text{ cm}^{-3}$

(b)  $n_e^{\text{Cu:ZnO NWs}} = 1.5 \times 10^{19} \text{ cm}^{-3}$

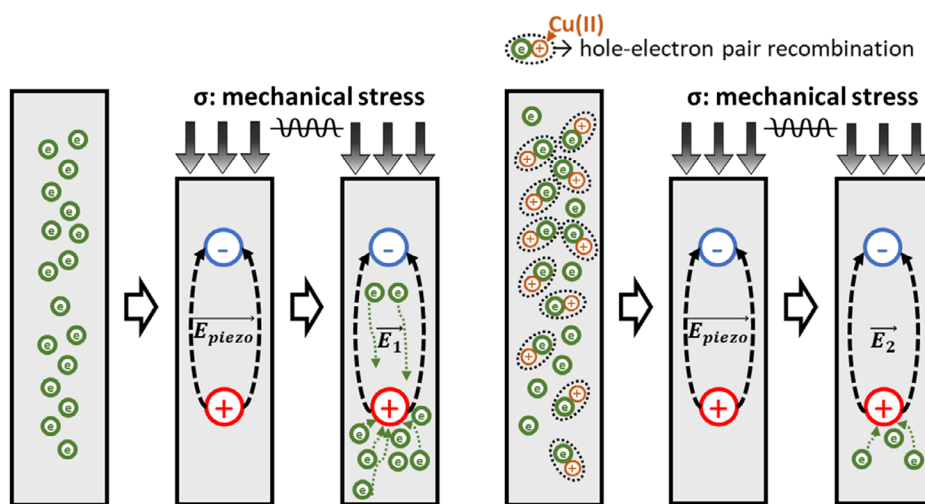


**Figure 7.** Electrical field generated in a) unintentionally n-doped and b) Cu-doped ZnO NW under mechanical stress ( $\vec{E}_1$  et  $\vec{E}_2$ , respectively). The  $\vec{E}_{\text{piezo}}$  refers to the spontaneous electrical field along the  $c$ -axis generated by the nonzero dipole moment induced in ZnO NWs under mechanical stress, as result of the movement of positively and negatively charged planes composed of zinc and oxygen atoms, respectively.<sup>[23]</sup> For unintentionally n-doped ZnO NWs, for which a higher density of free electrons ( $n_e$ ) than Cu-doped ZnO NWs is expected, a strongest screening potential occurs through electrostatic interactions between the created positive pole and free electrons. For Cu-doped ZnO NWs, by recombination of hole–electron pair, the density of free electrons reduces as well as the screening effect, leading to higher electrical field ( $|E_2| > |E_1|$ ). Hence, when the PNG is connected to an external load, more external charges are attracted by  $\vec{E}_2$ , resulting in enhanced output voltages of PNG-B.

### 3. Conclusion

In the present work, Cu-doped ZnO NWs have been grown by CBD in a high-pH region using  $\text{Cu}(\text{NO}_3)_2$  and  $\text{NH}_3$  as chemical additives, and their structural morphology and electrical properties have been compared to the one of unintentionally n-doped ZnO NWs. The vertically aligned unintentionally n- and Cu-doped ZnO NWs have subsequently been subjected to a thermal annealing under oxygen atmosphere for 1 h at 300, 500, and 800 °C. Notably, the Cu-doped ZnO NWs exhibit flat hexagonal shape top faces while unintentionally doped ZnO NWs have tapered shape top faces, both of them keeping their structural morphology after thermal annealing. The Raman spectroscopy analysis has demonstrated the formation of pure ZnO NWs excluding the formation of  $\text{Cu}_2\text{O}$  or  $\text{CuO}$  nanocrystals as residual phases, along with a change in the shape of the ZnO-related  $E_2^{\text{high}}$  peak, probably induced by a phonon contribution alteration resulting from a lattice distortion. The lattice distortion of ZnO NWs may be attributed to the redistribution of hydrogen- and nitrogen-related defects, as well as the Cu dopants, with respect to the annealing temperature. Furthermore, XPS spectra and ICP-MS analysis has shown the successful incorporation of Cu dopants into ZnO NWs with an atomic  $[\text{Cu}]/[\text{Zn}]$  ratio ranging from 50 to 65 ppm, along with the subsequent migration of Cu dopants potentially changing its oxidation state into the bulk of ZnO NWs after thermal annealing. In addition, two-point probe electrical resistivity measurements have indicated a continuous increase in the electrical resistivity of unintentionally n-doped ZnO NWs as the annealing temperature increments, ranging from 4.8 m $\Omega$  cm for pristine NWs to  $1.6 \times 10^4$  m $\Omega$  cm at 800 °C. In the case of Cu-doped ZnO NWs, the incorporation of Cu dopants leads to a significant reduction of the density of free electrons, resulting in higher electrical resistivity values, ranging from 20.2 m $\Omega$  cm for pristine NWs to  $1.7 \times 10^7$  m $\Omega$  cm at 800 °C, indicating their thermal activation. These findings have promoted the development of a PNG based on a Cu-doped ZnO NW matrix, resulting in an improved output voltage. The present device has produced twice the output voltage of a PNG based on an unintentionally n-doped ZnO NW matrix when tested under soft mechanical forces applied at low frequencies. Consequently, the compensatory Cu doping has been proved to be an effective strategy for enhancing the piezoelectric properties of ZnO NWs by reducing the screening effect through the decrease of the density of free electrons. The resulting improvement of the effective piezoelectric coefficient  $d_{33}^{\text{eff}}$  originating from the compensatory Cu doping opens perspectives in the field of piezoelectric devices such as PNGs and pressure/strain sensors.

### 4. Experimental Section

**Seed Layer Deposition and Synthesis of ZnO NWs:** In order to deposit the polycrystalline ZnO seed layers, a solution consisting of 375 mM of zinc acetate dehydrate ( $\text{Zn}(\text{CH}_3\text{COO})_2 \cdot 2\text{H}_2\text{O}$ , Sigma–Aldrich) and 375 mM monoethanolamine (MEA, Sigma–Aldrich) mixed in pure ethanol was prepared and stirred for 12 h at 60 °C and then at room temperature. Afterward, pre-cleaned Si(100) substrates in ultrasonic bath with acetone and isopropyl alcohol were dipped into the solution under a controlled atmosphere (<14% hygrometry). Then, they were annealed on a hot plate at 300 °C for 10 min to evaporate the organic solvent and kept for 1 h at

500 °C in an oven under air to crystallize the ZnO seed layer (ZnO/Si). For the PNG fabrication, the same dip-coating process was employed to deposit the polycrystalline ZnO seed layers on Si substrates covered by a metallic stack, but the final crystallization step was obtained by keeping the sample at 300 °C for 2 h 30 min in an oven under air (ZnO/Metal/Si). To synthesize ZnO NWs by CBD, the ZnO/Si substrates were subsequently placed face down in sealed reactors containing a 150 mL aqueous solution of zinc nitrate hexahydrate ( $\text{Zn}(\text{NO}_3)_2 \cdot 6\text{H}_2\text{O}$ , Sigma–Aldrich) and HMTA (Sigma–Aldrich) with an equimolar concentration of 30 mM. In addition, 1.5 mM of copper nitrate hemipentahydrate ( $\text{Cu}(\text{NO}_3)_2 \cdot 2.5\text{H}_2\text{O}$ , Sigma–Aldrich) was added to the chemical bath to proceed with the Cu doping using a  $[\text{Cu}(\text{NO}_3)_2]/[\text{Zn}(\text{NO}_3)_2]$  ratio of 5%. The initial pH of the chemical bath at room temperature, denoted as  $\text{pH}_0$ , was set to 10.6 following the addition of ammonia ( $\text{NH}_3$ , Sigma–Aldrich). The sealed reactors were placed in a regular oven heated at 85 °C for 21 h. For the PNG fabrication, ZnO NWs were grown on ZnO/Metal/Si substrates, according the previously described CBD method. This involved employing a 50 mL aqueous solution of zinc nitrate hexahydrate and HMTA with an equimolar concentration of 50 mM, along with 2.5 mM of copper nitrate hemipentahydrate. The  $\text{pH}_0$  of the chemical bath was set to 10.6 by adding ammonia. The ZnO NW growth was achieved at 85 °C for 3 h. Finally, the pristine unintentionally n- and Cu-doped ZnO NWs ( $[\text{Cu}(\text{II})]/[\text{Zn}(\text{II})]_{\text{bath}}$  ratio of 0% and 5%, respectively) grown on ZnO/Si substrates were thermally annealed in a tubular furnace under  $\text{O}_2$  atmosphere for 1 h at the annealing temperatures of 300, 500, and 800 °C.

**Characterization Techniques:** The morphological properties of ZnO NWs were analyzed with a FEI Quanta 250 FESEM instrument. Raman spectroscopy was achieved using a Horiba/Jobin Yvon Labram spectrometer equipped with a liquid nitrogen-cooled CCD detector. A 514.5 nm excitation line of an  $\text{Ar}^+$  laser with a power on the sample surface lower than 1 mW was focused on a spot size of 1  $\mu\text{m}^2$  using a 50 $\times$  objective. A Si reference sample was used for the spectral calibration in wavenumber using the theoretical Raman line set to 520.7  $\text{cm}^{-1}$ . The acquisition of Raman spectra was achieved in the backscattering configuration, where the laser probes an array of ZnO NWs from the top. XPS spectra were performed on a customized Thermo Fisher Scientific Theta 300 system with a monochromatized Al K $\alpha$  source. Thermofisher Advantage software was used to analyze the data. The XPS spectra were referenced with the 1s neutral carbon peak at 284.8 eV. The chemical composition was determined with a NexION 1000 PERKIN ELMER ICP-MS instrument. The nebulizer and spray chamber were a MEINHARD plus Glass Type C and Glass Cyclonic at 2 °C, respectively. The He flow rates of nebulization, auxiliary, and plasma gas were 1.02 mL  $\text{min}^{-1}$ , 1.2 L  $\text{min}^{-1}$ , and 15 L  $\text{min}^{-1}$ , respectively. The RF power was set at 1450 W. A KED mode was used with 4 mL  $\text{min}^{-1}$  He (7%  $\text{H}_2$ ) as collision gas. The Si substrates were dipped into a 0.8% nitric acid solution [ $\text{HNO}_3$ , Carlo Erba] to dissolve ZnO NWs. The solution containing only the Si substrate was previously assayed to make sure that no contaminants are released during the preparation. The electrical resistivity measurements on single ZnO NWs were performed with a two-probe measurement station connected to a Keithley 4200A-SCS parametric analyzer. The implemented test bench for the piezoelectric characterizations of PNGs involved a SmartShaker K2007E01 (PCB Piezotronics) acting as a mechanical excitation source. A Keysight 33210A function generator supplied the shaker with an alternating electrical signal, which was converted into a mechanical vibration. The latter were transmitted to a mechanical arm attached to the shaker. Thus, the mechanical stress could present values from 0.5 to 30 N applied over an area of 0.2  $\text{cm}^2$  (i.e., from 25 kPa to 1.5 MPa) at different frequencies between 0.1 and 9000 Hz. This mechanical stress was measured in real-time by an ICP 208C02 (PCB Piezotronics) force sensor placed between the shaker and the mechanical arm with a sensitivity of 11.24 mV  $\text{N}^{-1}$ . Then, this sensor was connected to a ICP 480C02 (PCB Piezotronics) signal conditioner to optimize the transmitted signal. The piezoelectric signal generated by the PNG was gathered by a Stanford Research Systems SR560 amplifier in order to amplify it and/or filter the external noise signals. Finally, a Teledyne LeCroy T3DSO2304 oscilloscope displayed the electrical signals coming from the PNG and the force conditioner.



## Supporting Information

Supporting Information is available from the Wiley Online Library or from the author.

## Acknowledgements

This work was partially supported by LabEx MINOS under the contract ANR-10-LABX-55-01 and the French RENATECH network through the PTA technological platforms. M.M. held a doctoral fellowship from LabEx MINOS. V.C. also acknowledges the financial support from the French National Research Agency through the project IMINEN (ANR-22-CE09-0032). This research has also benefited from some of the characterization equipment of the Grenoble INP-CMTC platform and of IUT 1 Chemical Department platform.

## Conflict of Interest

The authors declare no conflict of interest.

## Data Availability Statement

The data that support the findings of this study are available from the corresponding author upon reasonable request.

## Keywords

chemical bath deposition, piezoelectric nanogenerators, ZnO nanowires

Received: November 2, 2023

Revised: January 19, 2024

Published online: February 14, 2024

- [1] Z. L. Wang, *Adv. Funct. Mater.* **2008**, *18*, 3553.
- [2] Y. Qin, X. Wang, Z. L. Wang, *Nature* **2008**, *451*, 809.
- [3] Z. L. Wang, *Nano Res.* **2008**, *1*, 1.
- [4] Z. Wang, L. Zhou, X. W. Lou, *Adv. Mater.* **2012**, *24*, 1903.
- [5] S. Veeralingam, S. Badhulika, *ACS Appl. Energy Mater.* **2022**, *5*, 12884.
- [6] H. Yu, Y. Zhu, L. Zhu, X. Lin, Q. Wan, *Front. Nanotechnol.* **2022**, *4*, 1.
- [7] J. Briscoe, S. Dunn, *Nano Energy* **2014**, *14*, 15.
- [8] S. S. Indira, C. A. Vaithilingam, K. S. P. Oruganti, F. Mohd, S. Rahman, *Nanomaterials* **2019**, *9*, 773.
- [9] X. Cao, Y. Xiong, J. Sun, X. Zhu, Q. Sun, Z. L. Wang, *Adv. Funct. Mater.* **2021**, *31*, 2102983.
- [10] D. Hu, M. Yao, Y. Fan, C. Ma, M. Fan, M. Liu, *Nano Energy* **2019**, *55*, 288.
- [11] R. Yang, Y. Qin, C. Li, G. Zhu, Z. L. Wang, *Nano Lett.* **2009**, *9*, 1201.
- [12] Z. Li, G. Zhu, R. Yang, A. C. Wang, Z. L. Wang, *Adv. Mater.* **2010**, *22*, 2534.
- [13] M. Lee, C. Y. Chen, S. Wang, S. N. Cha, Y. J. Park, J. M. Kim, L. J. Chou, Z. L. Wang, *Adv. Mater.* **2012**, *24*, 1759.
- [14] Y. Zhao, P. Deng, Y. Nie, P. Wang, Y. Zhang, L. Xing, X. Xue, *Biosens. Bioelectron.* **2014**, *57*, 269.
- [15] L. Zhang, Y. Fu, L. Xing, B. Liu, Y. Zhang, X. Xue, *J. Mater. Chem. C* **2017**, *5*, 6005.
- [16] Z. Zhao, Y. Dai, S. X. Dou, J. Liang, *Mater. Today Energy* **2021**, *20*, 100690.
- [17] L. Schmidt-Mende, J. L. MacManus-Driscoll, *Mater. Today* **2007**, *10*, 40.
- [18] L. Vayssieres, K. Keis, S. E. Lindquist, A. Hagfeldt, *J. Phys. Chem. B* **2001**, *105*, 3350.
- [19] K. M. McPeak, J. B. Baxter, *Cryst. Growth Des.* **2009**, *9*, 4538.
- [20] R. Bahramian, H. Eshghi, A. Moshaii, *Mater. Des.* **2016**, *107*, 269.
- [21] R. Parize, J. Garnier, O. Chaix-Pluchery, C. Verrier, E. Appert, V. Consonni, *J. Phys. Chem. C* **2016**, *120*, 5242.
- [22] J. Villafuerte, F. Donatini, J. Kioseoglou, E. Sarigiannidou, O. Chaix-Pluchery, J. Pernot, V. Consonni, *J. Phys. Chem. C* **2020**, *124*, 16652.
- [23] V. Consonni, A. M. Lord, *Nano Energy* **2021**, *83*, 105789.
- [24] G. Romano, G. Mantini, A. Di Carlo, A. D'Amico, C. Falconi, Z. L. Wang, *Nanotechnology* **2011**, *22*, 465401.
- [25] G. Tian, D. Xiong, Y. Su, T. Yang, Y. Gao, C. Yan, W. Deng, L. Jin, H. Zhang, X. Fan, C. Wang, W. Deng, W. Yang, W. Yang, *Nano Lett.* **2020**, *20*, 4270.
- [26] R. K. Pandey, J. Dutta, S. Brahma, B. Rao, C. P. Liu, *J. Phys. Mater.* **2021**, *4*, 044011.
- [27] J. B. Baxter, C. A. Schmuttenmaer, *J. Phys. Chem. B* **2006**, *110*, 25229.
- [28] A. M. Lord, T. G. Maffei, A. S. Walton, D. M. Kepaptsoglou, Q. M. Ramasse, M. B. Ward, J. Köble, S. P. Wilks, *Nanotechnology* **2013**, *24*, 435706.
- [29] C. Opoku, A. S. Dahiya, F. Cayrel, G. Poulin-Vittrant, D. Alquier, N. Camara, *RSC Adv.* **2015**, *5*, 69925.
- [30] L. Wang, S. Guillemin, J. M. Chauveau, V. Sallet, F. Jomard, R. Brenier, V. Consonni, G. Brémond, *Phys. Status Solidi C* **2016**, *13*, 576.
- [31] T. Cossuet, F. Donatini, A. M. Lord, E. Appert, J. Pernot, V. Consonni, *J. Phys. Chem. C* **2018**, *122*, 22767.
- [32] R. Hinchet, S. Lee, G. Ardila, L. Montès, M. Mouis, Z. L. Wang, *Adv. Funct. Mater.* **2014**, *24*, 971.
- [33] O. Synhaivskiy, D. Albertini, P. Gaffuri, J. M. Chauveau, V. Consonni, B. Gautier, G. Brémond, *J. Phys. Chem. C* **2021**, *125*, 15373.
- [34] A. J. Lopez Garcia, M. Mouis, V. Consonni, G. Ardila, *Nanomaterials* **2021**, *11*, 941.
- [35] Y. Hu, L. Lin, Y. Zhang, Z. L. Wang, *Adv. Mater.* **2012**, *24*, 110.
- [36] T. S. van den Heever, W. J. Perold, *Smart Mater. Struct.* **2013**, *22*, 105029.
- [37] K. Y. Lee, B. Kumar, J. Seo, K.-H. Kim, J. I. Sohn, S. N. Cha, D. Choi, Z. L. Wang, S. Kim, *Nano Lett.* **2012**, *12*, 1959.
- [38] S. H. Shin, M. H. Lee, J. Y. Jung, J. H. Seol, J. Nah, *J. Mater. Chem. C* **2013**, *1*, 8103.
- [39] K. C. Pradel, W. Wu, Y. Ding, Z. L. Wang, *Nano Lett.* **2014**, *14*, 6897.
- [40] J. Villafuerte, O. Chaix-Pluchery, J. Kioseoglou, F. Donatini, E. Sarigiannidou, J. Pernot, V. Consonni, *Phys. Rev. Mater.* **2021**, *5*, 056001.
- [41] Y. Sun, S. Shen, W. Deng, G. Tian, D. Xiong, H. Zhang, T. Yang, S. Wang, J. Chen, W. Yang, *Nano Energy* **2023**, *105*, 108024.
- [42] M. D. McCluskey, S. J. Jokela, *J. Appl. Phys.* **2009**, *106*, 071101.
- [43] O. Lupan, L. Chow, L. K. Ono, B. R. Cuenya, G. Chai, H. Khallaf, S. Park, A. Schulte, *J. Phys. Chem. C* **2010**, *114*, 12401.
- [44] S. H. Lee, J. S. Lee, W. B. Ko, J. I. Sohn, S. N. Cha, J. M. Kim, Y. J. Park, J. P. Hong, *Appl. Phys. Express* **2012**, *5*, 095002.
- [45] C. H. Park, S. B. Zhang, S. H. Wei, *Phys. Rev. B* **2002**, *66*, 073202.
- [46] E. Kaminska, I. Pasternak, P. Boguslawski, A. Jezierski, E. Dynowska, R. Jakiela, E. Przewdzicka, A. Piotrowska, J. Kossut, *AIP Conf. Proc.* **2009**, *1199*, 120.
- [47] M. A. Borysiewicz, *Crystals* **2019**, *9*, 505.
- [48] C. Lausecker, B. Salem, X. Baillin, O. Chaix-Pluchery, H. Roussel, S. Labau, B. Pelissier, E. Appert, V. Consonni, *Inorg. Chem.* **2021**, *60*, 1612.
- [49] Y. Yan, M. M. Al-Jassim, S. H. Wei, *Appl. Phys. Lett.* **2006**, *89*, 87.
- [50] D. Huang, Y. J. Zhao, D. H. Chen, Y. Z. Shao, *Appl. Phys. Lett.* **2008**, *92*, 90.



- [51] F. Wang, J. H. Seo, Z. Li, A. V. Kvit, Z. Ma, X. Wang, *ACS Appl. Mater. Interfaces* **2014**, *6*, 1288.
- [52] A. Baillard, E. Appert, M. Weber, V. Jacob, H. Roussel, L. Rapenne, O. Chaix-Pluchery, V. Consonni, *J. Phys. Chem. C* **2023**, *127*, 8306.
- [53] A. Baillard, E. Appert, M. Weber, V. Jacob, H. Roussel, L. Rapenne, O. Chaix-Pluchery, V. Consonni, *Inorg. Chem.* **2023**, *62*, 1165.
- [54] M. Valtiner, S. Borodin, G. Grundmeier, *Langmuir* **2008**, *24*, 5350.
- [55] S. Guillemin, V. Consonni, E. Appert, E. Puyoo, L. Rapenne, H. Roussel, *J. Phys. Chem. C* **2012**, *116*, 25106.
- [56] W. Dai, X. Pan, C. Chen, S. Chen, W. Chen, H. Zhang, Z. Ye, *RSC Adv.* **2014**, *4*, 31969.
- [57] R. Cuscó, E. Alarcón-Lladó, J. Ibáñez, L. Artús, J. Jiménez, B. Wang, M. J. Callahan, *Phys. Rev. B* **2007**, *75*, 165202.
- [58] Y. Deng, A. D. Handoko, Y. Du, S. Xi, B. S. Yeo, *ACS Catal.* **2016**, *6*, 2473.
- [59] C. Bundesmann, N. Ashkenov, M. Schubert, D. Spemann, T. Butz, E. M. Kaidashev, M. Lorenz, M. Grundmann, *Appl. Phys. Lett.* **2003**, *83*, 1974.
- [60] J. Villafuerte, E. Sarigiannidou, F. Donatini, J. Kioseoglou, O. Chaix-Pluchery, J. Pernot, V. Consonni, *Nanoscale Adv.* **2022**, *4*, 1793.
- [61] P. Sundara Venkatesh, V. Ramakrishnan, K. Jeganathan, *Phys. B* **2016**, *481*, 204.
- [62] O. Lupan, T. Pauporté, T. Le Bahers, B. Viana, I. Ciofini, *Adv. Funct. Mater.* **2011**, *21*, 3564.
- [63] S. Sahoo, G. L. Sharma, R. S. Katiyar, *J. Raman Spectrosc.* **2012**, *43*, 72.
- [64] C. L. Hsu, Y. D. Gao, Y. S. Chen, T. J. Hsueh, *ACS Appl. Mater. Interfaces* **2014**, *6*, 4277.
- [65] K. Samanta, P. Bhattacharya, R. S. Katiyar, W. Iwamoto, P. G. Pagliuso, C. Rettori, *Phys. Rev. B* **2006**, *73*, 245213.
- [66] M. C. Biesinger, *Surf. Interface Anal.* **2017**, *49*, 1325.
- [67] J. Sultana, S. Paul, A. Karmakar, G. K. Dalapati, S. Chattopadhyay, *J. Mater. Sci.: Mater. Electron.* **2018**, *29*, 12878.
- [68] N. Y. Garces, L. Wang, L. Bai, N. C. Giles, L. E. Halliburton, G. Cantwell, *Appl. Phys. Lett.* **2002**, *81*, 622.
- [69] P. Gaffuri, T. Dedova, E. Appert, M. Danilson, A. Baillard, O. Chaix-Pluchery, F. Güell, I. Oja-Acik, V. Consonni, *Appl. Surf. Sci.* **2022**, *582*, 152323.
- [70] A. Soudi, C. H. Hsu, Y. Gu, *Nano Lett.* **2012**, *12*, 5111.
- [71] A. De Luna Bugallo, F. Donatini, C. Sartet, V. Sallet, J. Pernot, *Appl. Phys. Express* **2015**, *8*, 025001.
- [72] C. Soci, A. Zhang, B. Xiang, S. A. Dayeh, D. P. R. Aplin, J. Park, X. Y. Bao, Y. H. Lo, D. Wang, *Nano Lett.* **2007**, *7*, 1003.
- [73] A. M. Lord, T. G. Maffei, M. W. Allen, D. Morgan, P. R. Davies, D. R. Jones, J. E. Evans, N. A. Smith, S. P. Wilks, *Appl. Surf. Sci.* **2014**, *320*, 664.
- [74] C. West, D. J. Robbins, P. J. Dean, W. Hayes, *Physica B+C* **1983**, *116*, 492.
- [75] J. V. Bellini, M. R. Morelli, R. H. G. A. Kiminami, *J. Mater. Sci.: Mater. Electron.* **2002**, *13*, 485.
- [76] R. Shabannia, *J. Mater. Sci.: Mater. Electron.* **2018**, *29*, 11646.
- [77] H. L. Pan, B. Yao, T. Yang, Y. Xu, B. Y. Zhang, W. W. Liu, D. Z. Shen, *Appl. Phys. Lett.* **2010**, *97*, 2.
- [78] V. L. Patil, S. A. Vanalakar, N. L. Tarwal, A. P. Patil, T. D. Dongale, J. H. Kim, P. S. Patil, *Sens. Actuators, A* **2019**, *299*, 111611.
- [79] C. Chen, W. Dai, Y. Lu, H. He, Q. Lu, T. Jin, Z. Ye, *Mater. Res. Bull.* **2015**, *70*, 190.
- [80] M. Suja, S. B. Bashar, M. M. Morshed, J. Liu, *ACS Appl. Mater. Interfaces* **2015**, *7*, 8894.
- [81] A. Furukawa, N. Ogasawara, R. Yokozawa, T. Tokunaga, *Jpn. J. Appl. Phys.* **2008**, *47*, 8799.
- [82] S. Brochen, G. Feuillet, J. L. Sentailler, R. Obrecht, M. Lafossas, P. Ferret, J. M. Chauveau, J. Pernot, *J. Appl. Phys.* **2017**, *121*, 095704.
- [83] W. F. Gorham, *J. Polym. Sci., Part A: Polym. Chem.* **1966**, *4*, 3027.
- [84] O. Graton, G. Poulin-Vittrant, A. S. Dahiya, N. Camara, L. P. T. H. Hue, M. Lethiecq, *Phys. Status Solidi RRL* **2013**, *7*, 915.
- [85] A. Pachi, T. Ji, *Struct. Eng.* **2005**, *83*, 36.
- [86] A. S. Bugaev, V. V. Chapursky, S. I. Ivashov, V. V. Razevig, A. P. Sheyko, I. A. Vasilyev, in *Proc. Tenth Int. Conf. Gr. Penetrating Radar, GPR 2004*, Vol. 1, **2004**, pp. 291–294.
- [87] C. B. Irwin, M. E. Sesto, *Appl. Ergon.* **2012**, *43*, 1038.
- [88] C. Wan, C. R. Bowen, *J. Mater. Chem. A* **2017**, *5*, 3091.
- [89] R. Yang, Y. Qin, L. Dai, Z. L. Wang, *Nat. Nanotechnol.* **2009**, *4*, 34.
- [90] K. Il Park, S. Bin Bae, S. H. Yang, H. I. Lee, K. Lee, S. J. Lee, *Nanoscale* **2014**, *6*, 8962.
- [91] A. J. Lopez Garcia, R. Tao, M. Mouis, G. Ardila, in *21st Int. Conf. Solid-State Sensors, Actuators Microsystems, TRANSDUCERS 2021* **2021**, pp. 1056–1059.
- [92] E. Broitman, M. Y. Soomro, J. Lu, M. Willander, L. Hultman, *Phys. Chem. Chem. Phys.* **2013**, *15*, 11113.
- [93] D. A. Scrymgeour, J. W. P. Hsu, *Nano Lett.* **2008**, *8*, 2204.